

## AM–FM Texture Segmentation in Electron Microscopic Muscle Imaging

Marios S. Pattichis\*, Constantinos S. Pattichis, Maria Avraam, Alan Bovik, and Kyriacos Kyriacou

**Abstract**—This paper describes the application of an amplitude modulation–frequency modulation (AM–FM) image representation in segmenting electron micrographs of skeletal muscle for the recognition of: 1) normal sarcomere ultrastructural pattern and 2) abnormal regions that occur in sarcomeres in various myopathies. A total of 26 electron micrographs from different myopathies were used for this study. It is shown that the AM–FM image representation can identify normal repetitive structures and sarcomeres, with a good degree of accuracy. This system can also detect abnormalities in sarcomeres which alter the normal regular pattern, as seen in muscle pathology, with a recognition accuracy of 75%–84% as compared to a human expert.

**Index Terms**—AM–FM modeling, electron microscopy, muscle imaging, myopathies, texture analysis.

### I. INTRODUCTION

Accurate diagnosis of neuromuscular disorders often requires examination of muscle biopsies with both light and electron microscopes. Ultrastructural examination is useful for confirming the diagnosis of specific disease entities, such as congenital, vacuolar, and metabolic myopathies [1], [2]. Most of these myopathies are characterized by the abnormal accumulation of various types of structures, such as nemaline rods, tubular aggregates, or vacuoles. These structures disturb the very regular and repetitive sarcomere pattern of myofibers. The sarcomeres are the basic functional units of myofibers and the microscopical recognition and precise description of abnormal structures provides the basic criteria for classifying certain myopathies.

In recent years, in order to increase the diagnostic value of electron microscopic observations, muscle morphometry has also been introduced. Although this has been found useful for providing important supplementary diagnostic information [3], it still relies on the precise recognition of abnormal structures by a human expert. In order to assist the human expert in this recognition task, a novel amplitude modulation–frequency modulation (AM–FM) image representation method has been developed for segmenting electron microscopic muscle images. The main objective is to develop a system capable of recognizing structural abnormalities that affect the regular sarcomere arrangement of muscle fibers.

Manuscript received May 17, 1999; revised September 22, 2000. This work was supported in part by the Cyprus Institute of Neurology and Genetics Telethon funds. The Associate Editor responsible for coordinating the review of this paper and recommending its publication was M. W. Vannier. *Asterisk indicates corresponding author.*

\*M. S. Pattichis is with the Department of Electrical and Computer Engineering, The University of New Mexico, Albuquerque, NM 87131 USA (e-mail: pattichis@ece.unm.edu).

C. S. Pattichis and M. Avraam are with the Department of Computer Science, University of Cyprus, P.O. Box 20537, Nicosia, Cyprus (e-mail: pattichi@ucy.ac.cy).

A. Bovik is with the Department of Electrical and Computer Engineering, University of Texas, Austin, TX 78712-1084 USA (e-mail: bovik@vision.ece.utexas.edu).

K. Kyriacou is with the Department of Electron Microscopy, The Cyprus Institute of Neurology and Genetics, P.O. Box 3462, Nicosia, Cyprus (e-mail: kyriacos@mdrtc.cing.ac.cy).

Publisher Item Identifier S 0278-0062(00)10883-3.

## II. AM–FM METHOD

### A. Skeletal Muscle Ultrastructure

Normal skeletal muscle consists of sarcomeres; these are microscopic functional units that are being repeated horizontally, along muscle fibers. In addition, the sarcomeres are vertically aligned and contain thin filaments of actin and thick filaments of myosin. The borders of the sarcomeres, are delimited by Z lines, which line up in adjacent myofibrils giving rise to the typical striated appearance of skeletal muscle [Fig. 1(a)]. The actin filaments are attached to the Z line while the myosin filaments are centered in the sarcomere. The actin filaments do not extend completely across the sarcomere, so the H-zone, in the center of the A-band contains only myosin filaments. This arrangement of myofilaments creates a repeating pattern of light I-bands and dark A-bands [Fig. 1(a)].

### B. Material

Muscle biopsies were obtained and processed for transmission electron microscopy according to standard protocols [4]. For this study, electron micrographs obtained from a normal biopsy, and others obtained from three different types of myopathy—outlined below—were used.

- *Normal*: Fig. 1(b) illustrates an electron micrograph of normal human skeletal muscle showing the regular sarcomere structure.
- *Nemaline Myopathy*: Fig. 2(a) illustrates an electron micrograph of a longitudinal section from skeletal muscle showing the presence of nemaline rods. These are abnormal structures which occur in a number of myopathies but are pathognomonic for the diagnosis of nemaline myopathies. It should be noted that nemaline myopathy is a rare disease, altogether ten electron micrographs from different muscle fibers of two such cases were used.
- *Tubular Aggregates Myopathy*: Fig. 2(b) illustrates an electron micrograph of a longitudinal section from skeletal muscle which shows accumulation of tubular aggregates. These tubules accumulate in sarcomeres causing disruption of the regular sarcomere pattern. In this case, we used six electron micrographs from different muscle fibers of the biopsy from one patient.
- *Mitochondrial Myopathy*: Fig. 2(c) illustrates an electron micrograph of a longitudinal section from skeletal muscle showing accumulation of mitochondria. Although mitochondria are normally present in sarcomeres, the finding of mitochondrial aggregates is often a characteristic and significant finding in mitochondrial myopathies. For this part of the work, ten electron micrographs, obtained from four different cases, diagnosed as mitochondrial myopathies were used.

For each digitized electron micrograph, included in the study, the pathological region was manually segmented by the expert using MATLAB.

### C. AM–FM Series

In electron micrographs of human skeletal muscle, sarcomere units appear periodically arranged. Since these images are nearly periodic, and we know that every periodic image is fully described by a two-dimensional (2-D) Fourier series, it is natural to consider a Fourier series expansion for describing these images. Naturally, the periodicity is broken over abnormal regions. We, thus, modify the Fourier series expansion to account for these variations. After the modifications, the Fourier series becomes an AM–FM series. We will next develop these points in a step by step approach.

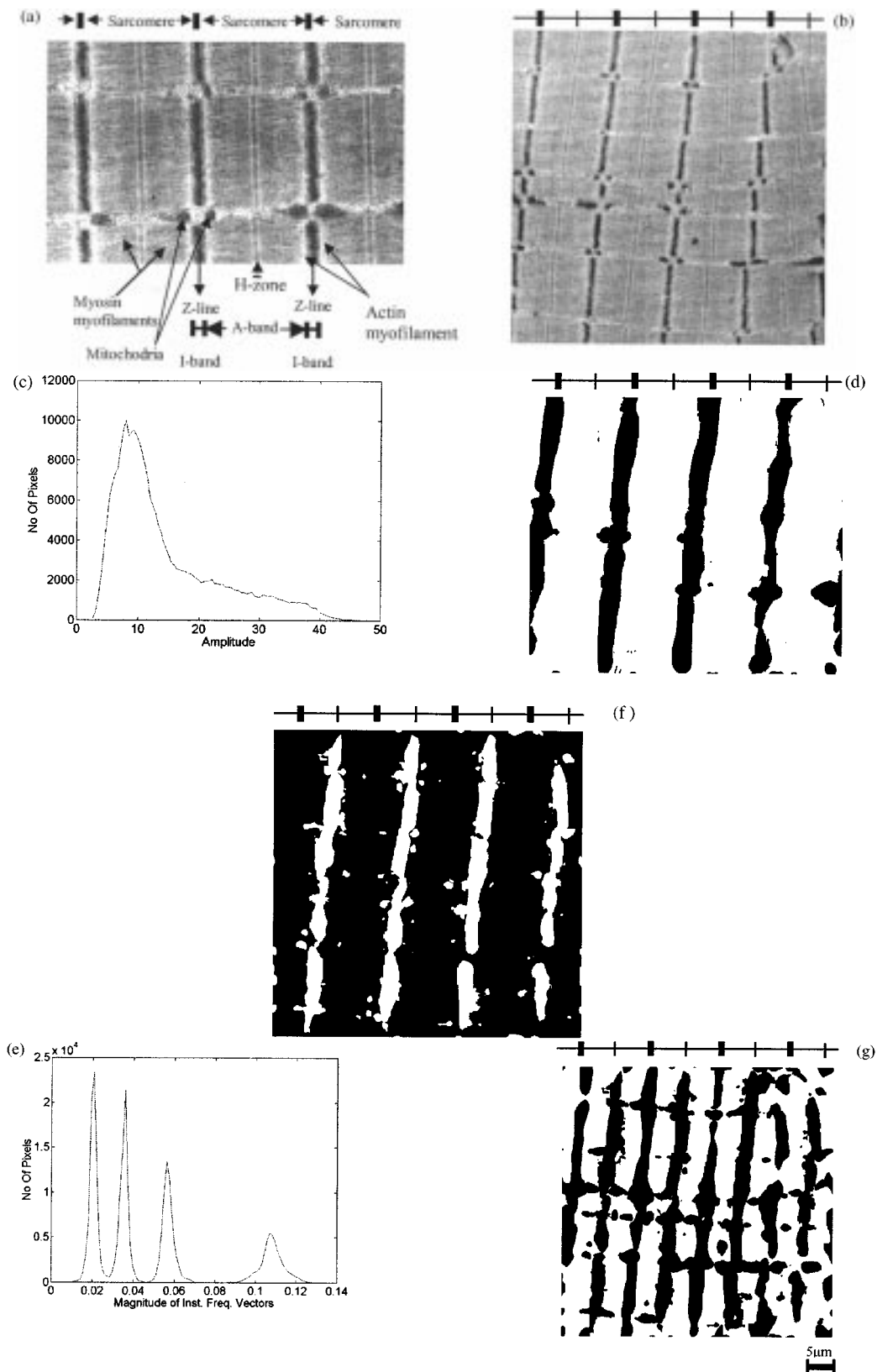


Fig. 1. (a) Annotated electron micrograph of human skeletal muscle. (b) Electron micrograph of normal human skeletal muscle (Magnification 10 000). Results of AM-FM analysis of image in (b): (c) AM-FM amplitude histogram. (d) The result of thresholding the amplitude at  $a(x) < 20$ . (e) AM-FM instantaneous frequency magnitude. (f) The result for thresholding the instantaneous frequency for low magnitudes at  $\|\nabla\Phi_{i,j}(x)\| < 0.046$  cycles per image length. (g) The result for thresholding the instantaneous frequency at higher magnitudes  $0.08 < \|\nabla\Phi_{i,j}(x)\| < 0.15$  cycles per image length. (Thick bar = Z lines: sarcomere boundaries. Thin bar = H-zone: mid-regions of sarcomeres).

Let  $T_1$  be the horizontal length for a sarcomere unit, and  $T_2$  be the vertical length of a sarcomere unit. Muscle images can be expressed as periodic satisfying

$$I_{\text{normal}}(x_1, x_2) = I_{\text{normal}}(x_1 + T_1, x_2 + T_2) \quad (1)$$

Hence, the image may be expanded into its Fourier series

$$I_{\text{normal}}(x_1, x_2) = \sum_{n, m} A_{n, m} \exp \left[ j2\pi \left( \frac{n}{T_1} x_1 + \frac{m}{T_2} x_2 \right) \right] \quad (2)$$

In electron micrographs [see Fig. 1(b)], the sarcomere regions are modeled as normal regions that have undergone slight local variations due to biological activity and function. These slight variations are modeled by a coordinate transformation from the normal image coordinates of  $x_1 - x_2$  to the deformed image coordinates  $\phi_1(x_1, x_2) - \phi_2(x_1, x_2)$ . Furthermore, subtle variations in the sarcomere image intensity are modeled by multiplying the coordinate-transformed image by an amplitude function  $a_{sar}(x_1, x_2)$ . A regular sarcomere image is expressed as [set  $\mathbf{x} = (x_1, x_2)$ ] [5]

$$\begin{aligned} I_{sar}(\mathbf{x}) &= a_{sar}(\mathbf{x}) I_{\text{normal}}(\phi_1(\mathbf{x}), \phi_2(\mathbf{x})) \\ &= a_{sar}(\mathbf{x}) \sum_{n, m} A_{n, m} \\ &\quad \cdot \exp \left[ j2\pi \left( \frac{n}{T_1} \phi_1(\mathbf{x}) + \frac{m}{T_2} \phi_2(\mathbf{x}) \right) \right]. \end{aligned} \quad (3)$$

The gradient of the phase function

$$\nabla 2\pi \left( \frac{n}{T_1} \phi_1(\mathbf{x}) + \frac{m}{T_2} \phi_2(\mathbf{x}) \right) = \frac{2n\pi}{T_1} \nabla \phi_1(\mathbf{x}) + \frac{2m\pi}{T_2} \nabla \phi_2(\mathbf{x})$$

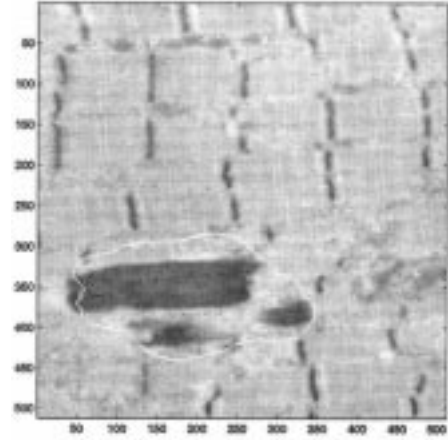
is called the ‘‘instantaneous-frequency’’ of the FM function  $\exp\{j2\pi[(n/T_1)\phi_1(\mathbf{x}) + (m/T_2)\phi_2(\mathbf{x})]\}$ . To avoid confusion among the indexes, we note that the phase subscripts refer to the vector components (one for first, and two for second), while the double indexes in  $A_{n, m}$  refer to the AM-FM harmonics.

For an abnormal case, some of the image regions deviate significantly from the regular sarcomere pattern. To account for these regions, we introduce a new amplitude function  $a_{\text{abnormal}}$  and a new curvilinear coordinate system  $\psi_1 - \psi_2$ . We rewrite (3) as

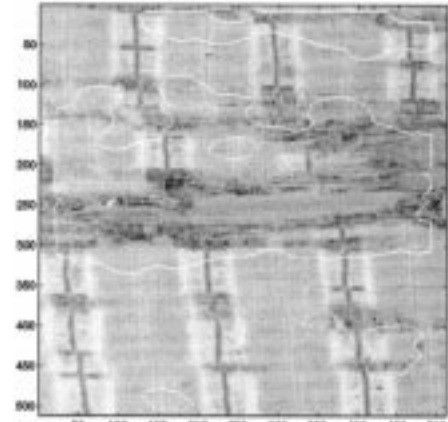
$$\begin{aligned} I(\mathbf{x}) &= a_{sar}(\mathbf{x}) \sum_{n, m} A_{n, m} \\ &\quad \cdot \exp \left[ j2\pi \left( \frac{n}{T_1} \phi_1(\mathbf{x}) + \frac{m}{T_2} \phi_2(\mathbf{x}) \right) \right] \\ &\quad + a_{\text{abnormal}}(\mathbf{x}) \sum_{n, m} B_{n, m} \\ &\quad \cdot \exp \left[ j2\pi \left( \frac{n}{T_1} \psi_1(\mathbf{x}) + \frac{m}{T_2} \psi_2(\mathbf{x}) \right) \right] \end{aligned} \quad (4)$$

where the first summation describes the image over normal regions, while the second summation describes the image over the abnormal regions. In (4), we note that at any given pixel, only one of the two amplitude functions is nonzero. If a pixel belongs to a normal region, then the normal amplitude is nonzero:  $a_{sar}(\mathbf{x}) \neq 0$ , while the abnormal amplitude is zero:  $a_{\text{abnormal}}(\mathbf{x}) = 0$ . Conversely, if a pixel is part of an abnormal region:  $a_{sar}(\mathbf{x}) = 0$ ,  $a_{\text{abnormal}}(\mathbf{x}) \neq 0$ .

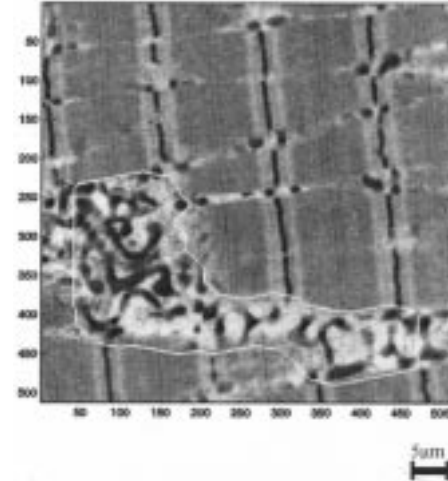
Using (4), an arbitrary electron microscopic muscle image can be described in terms of the amplitude functions:  $a_{sar}$ ,  $a_{\text{abnormal}}$ , the phase functions:  $\phi_1$ ,  $\phi_2$ ,  $\psi_1$ ,  $\psi_2$  and the AM-FM series coefficients:



(a)



(b)



(c)

Fig. 2. AM-FM segmented electron micrographs: (a) nemaline myopathy, (b) tubular aggregates myopathy, and (c) mitochondrial myopathy. (Magnification 10 000).

$A_{n, m}$ ,  $B_{n, m}$ . To segment the image into sarcomeres and abnormal regions, we estimate  $a_{sar}$ ,  $a_{\text{abnormal}}$ , and the instantaneous frequency magnitude functions:  $\|\nabla \phi_1\|$ ,  $\|\nabla \psi_1\|$ . The instantaneous frequency magnitudes associated with the second curvilinear coordinates:  $\|\nabla \phi_2(\mathbf{x})\|$  and  $\|\nabla \psi_2(\mathbf{x})\|$  are not used. To estimate these functions, we use dominant component analysis (DCA) [6]–[8] as described in the following subsections.

#### D. Isolating the Fundamental AM–FM Components

It is expected that most of the “local” power is captured in the fundamental AM–FM components. Without loss of generality, let  $n = 1$ , and  $m = 0$  be the indexes of the fundamental components that dominate:

$$\begin{aligned} A_{1,0} a_{sar}(\mathbf{x}) \exp \left[ j \frac{2\pi}{T_1} \phi_1(\mathbf{x}) \right] \\ B_{1,0} a_{abnormal}(\mathbf{x}) \exp \left[ j \frac{2\pi}{T_1} \psi_1(\mathbf{x}) \right] \end{aligned} \quad (5)$$

in the sense that

$$\begin{aligned} |A_{1,0}| > |A_{n,m}| & \quad \text{for } (n, m) \neq (1, 0) \\ |B_{1,0}| > |B_{n,m}| & \quad \text{for } (n, m) \neq (1, 0). \end{aligned} \quad (6)$$

In practice, this assumption [see (6)] was satisfied for the cases that were investigated in this study. To verify that the fundamental AM–FM harmonic was actually computed, we compared the “instantaneous period” of the estimated harmonics against the original electron microscopic images. They were found to share similar wavelength values.

For simplicity, and without loss of generality, we will assume that fundamental coefficients  $A_{1,0}$  and  $B_{1,0}$  are both one (e.g., absorb the first harmonic coefficients into the amplitude functions, and rescale the rest of the harmonic coefficients).

#### E. Estimating the Fundamental AM–FM Component

The DCA algorithm is presented in this subsection as documented in [6], [7]. The DCA algorithm is spatially adaptive. At every pixel in the image, estimates of the amplitude, phase, and instantaneous frequency are obtained from a Gabor channel filter that gives the maximum response over a bank of channel filters.

In order to use the DCA algorithm to estimate the appropriate AM–FM harmonics [as described by (5)], we rely on the fundamental assumption stated in (6). Then, at every pixel  $\mathbf{x}_0$  belonging to the normal regions, we expect the Gabor channel filter with a frequency response closer to  $(2\pi/T_0)\nabla\phi_1(\mathbf{x}_0)$  to dominate (in the sense of capturing more power) than any other channel. On the other hand, at every pixel  $\mathbf{x}_1$  belonging to an abnormal region, we expect the Gabor channel filter with frequency response closer to  $(2\pi/T_1)\nabla\psi_1(\mathbf{x}_1)$ , to dominate. Hence, over the normal region, the dominant Gabor channel estimates the fundamental sarcomere harmonic:  $a_{sar}(\mathbf{x}) \exp[j(2\pi/T_1)\phi_1(\mathbf{x})]$ . Similarly, over the abnormal region, the dominant Gabor channel estimates the fundamental abnormal harmonic:  $a_{abnormal}(\mathbf{x}) \exp[j(2\pi/T_1)\psi_1(\mathbf{x})]$ . Hence, by selecting the suitable Gabor channel at every pixel, DCA does not depend on specific parameters of the image (e.g., it does not require knowledge of  $T_1$  and  $T_2$ ).

Next, we provide more details on the bank of Gabor channels, and how each channel is used to estimate the parameters. First, a highpass filter is applied that removes the low-frequency components. This is accomplished by: 1) filtering the image with a lowpass filter that is supported within a circular disk centered at the origin of the frequency plane and 2) subtracting the lowpass filtered image from the original image. A collection of Gabor (bandpass) channel filters are applied to the new, [highpass filtered] image. (Hence, the low-frequency components were significantly reduced (due to both highpass and bandpass filtering)). The Gabor channel filters are chosen so as to cover the 2-D frequency plane. Over each channel, estimates of the instantaneous frequency and amplitude are obtained using the equations given in [6]–[8].

#### F. Segmentation Based on the AM–FM Parameters

After estimating the fundamental AM–FM components, the estimated AM–FM parameters are used to extract the abnormal regions

from its background. The same segmentation procedure is applied to all the cases, but different AM–FM parameters were used for different myopathies. The AM–FM parameters are: 1) the amplitude (for mitochondria and nemaline myopathy cases) and 2) the angle of the instantaneous frequency vector (for tubular myopathy cases). An initial segmentation of the image is then computed using maximum likelihood. The final segmented image is computed from the initial, binary image using a morphological filter. We will next explain these two steps in more detail.

First, we explain the maximum likelihood step. Let  $z$  denote the AM–FM segmentation variable. Using the training set as ground truth, we compute  $p(1)$  denoting the probability of abnormal pixels,  $p(2)$  the probability of normal pixels, and the conditional probabilities:  $p(z|1)$  and  $p(z|2)$ . The probability density functions were averaged over the training set. On the test set, an image pixel is classified as abnormal if  $p(z|1)p(1) > p(z|2)p(2)$ , else, it is classified as normal.

The initial segmentation image is then modeled as a noisy binary image that needs to be denoised. Denoising is achieved via the use of an alternating sequential filter (ASF) (to be defined next). To help determine an appropriate ASF filter, we compute and then compare: 1) the average granulometric size distribution of the training set and 2) the granulometric size distribution of the particular test image. We will next define each morphological term in more detail.

A granulometric filter is defined by [9], [10]

$$M = (((((I \circ B) \circ 2B) \circ 3B) \circ 4B) \cdots) \circ nB \quad (9)$$

where

- $B$  structural element;
- $nB$  result of  $n$  dilations of  $B$  by itself;
- $\circ$  standard open operation.

We select a structural element  $B$  that favors abnormal components that extend horizontally (an ellipsoidal disk)

$$B = \{(i, j) | (i/7)^2 + (j/3)^2 \leq 1\}.$$

We compute the probability density function of the granulometric size distribution using the filter described in (9) (see [9] and [10] for details).

We assume that the noise in the segmented image is due to small structural components that do not belong to the abnormal regions. Under this assumption, it can be shown that the optimal morphological filter will be an ASF defined by [11], [12]

$$M = ((((((I \circ B) \bullet B) \circ 2B) \bullet 2B) \cdots) \circ nB) \bullet nB \quad (10)$$

where  $\bullet$  denotes the close operation. In (10), the value of  $n$  needs to be chosen so that the smaller, noisy structures are removed, while the larger structures are preserved. To choose  $n$ , the granulometric size distribution is computed for the test image. Then  $n$  is chosen as the number of times where the training set’s size distribution (where we have dropped the word granulometric), first exceeds the test image’s size distribution. Next, we explain why this approach works.

The test image is noisy and, hence, it has a larger number of small components, while the average distribution from the training images has a larger number of large components. This implies that the test image’s size distribution dominates (maintains larger values than) that of the training set’s, for the smaller, noisy components. Furthermore, the training set’s size distribution dominates the one of the test image’s for the larger components, where the signal is. It, hence, makes sense to set  $n$  to the value where the training set’s size distribution exceeds the test image’s size distribution, since this choice will most likely reject the noise in the image.

The electron micrographs were separated into training and evaluation (or test) sets, by running five, randomly selected, sets in each disease entity. In order to evaluate the performance of the AM–FM texture

TABLE I  
RECOGNITION ACCURACY OF THE AM-FM TEXTURE SEGMENTATION METHOD

	Type of myopathy		
	Nemaline	Tubular Aggregates	Mitochondrial
Number of cases	2	1	4
Number of regions	10	6	10
Recognition accuracy	84%	78%	75%

segmentation method, its recognition accuracy was compared to that of the human expert. For this purpose, the area recognized by the expert was used as the “gold standard.” For each region, this was compared to the area segmented by the system to calculate the system’s percentage recognition accuracy. This value was computed as the mean of the five evaluation sets in each type of myopathy.

### III. RESULTS

#### A. Normal Muscle

In Fig. 1(b)–(g), the results of AM-FM analysis for the normal case are displayed. For illustration purposes, on top of each image the horizontal line depicts a single muscle fiber. The sarcomere boundaries, Z lines, are represented by thick perpendicular bars, and the mid-sarcomere regions, H-zones, are represented by the thin perpendicular bars. The amplitude histogram of the AM-FM fundamental transform is shown in Fig. 1(c). The result of thresholding the original electron micrograph image [Fig. 1(b)] at  $a(x) < 20$  is given in Fig. 1(d). To help explain the results, it is noted that the amplitude of the AM-FM harmonic defines the maximum range of the image intensity ( $\pm a(\cdot)$ ). Fig. 1(d) displays the Z-bands as continuous dark vertical stripes (minimum intensity, also characterized by small amplitude values) while the remaining sarcomere regions appear white (nearly maximum intensities, also characterized by large amplitude values). The instantaneous frequency magnitude histogram is given in Fig. 1(e). It is noted that the frequency instantaneous magnitude is inversely proportional to the period of the locally repeating pattern (instantaneous wavelength). Fig. 1(f) was thresholded for low instantaneous frequency magnitude at  $\|\nabla\Phi_{i,j}(x)\| < 0.046$  cycles per image length. It highlights (white stripes) the sarcomere centers corresponding to the mid-regions of the A-bands, with the rest of the sarcomeres appearing black. Fig. 1(g) was thresholded at larger instantaneous frequency magnitudes,  $0.08 < \|\nabla\Phi_{i,j}(x)\| < 0.15$  cycles per image length. It is the composite of Fig. 1(d) and (f) illustrating the boundaries as well as the mid-regions of sarcomeres.

#### B. Nemaline Myopathy

Fig. 2(a) illustrates an electron micrograph of a case of nemaline myopathy. It is observed that there is a sharp intensity variation between the white background and the darker, nemaline regions. This results in a large amplitude over the nemaline regions (to account for the large variation in image intensity). Hence, the amplitude parameter was used in the automated AM-FM segmentation procedure.

In this myopathy, two cases were investigated, from which ten different regions were analyzed. Five of these regions were used for training the system, and five for performance evaluation. The average percentage recognition accuracy for the evaluation set of five trials was 84% (see Table I).

#### C. Tubular Aggregates Myopathy

A case of tubular aggregates myopathy is shown in Fig. 2(b). Upon close examination, it is observed that the tubular aggregates are dominated by vertically repeating, thinly spaced patterns as opposed to the horizontally repeating patterns of the normal background. This observation allows us to use the instantaneous frequency angle as the AM-FM parameter for the automated segmentation procedure.

In this rare myopathy, six different regions were studied, using three regions for training and three for evaluation. The average percentage recognition accuracy for the five trials was 78% (see Table I).

#### D. Mitochondrial Myopathy

Fig. 2(c) illustrates a case of mitochondrial myopathy. As in the nemaline myopathy cases, it is observed that there is a sharp intensity variation between the white background surrounding the mitochondria and the black color density of the mitochondria themselves. As a result, abnormal regions are characterized by a large amplitude to account for the white to black and black to white transitions. This observation justifies the use of the amplitude parameter for the automated segmentation procedure.

Four cases of mitochondrial myopathy were used from which ten regions were processed. Five of these regions were used for training and five for performance evaluation. The average percentage recognition accuracy for the evaluation set for five trials was 75% (see Table I).

### IV. CONCLUDING REMARKS

The results of this study suggest that the application of AM-FM texture segmentation in electron microscopic muscle imaging can identify normal repetitive structures with a good degree of accuracy. Furthermore, this AM-FM texture segmentation is capable of detecting abnormal regions which disturb the regular sarcomere pattern of myofibers. This is a novel approach since the task of recognizing abnormalities in myofibers is currently carried out manually by human experts. Although a small number of regions was studied, the system’s performance recognition accuracy was found to be relatively good, ranging from 75% to 84%.

More work is currently being carried out in order to make the AM-FM recognition system more accurate. The wider applicability of this technology will also enhance the cell biologist’s or neuropathologist’s ability to recognize and quantify similar changes that alter the repetitive cellular patterns at the ultrastructural level. This AM-FM method has been successful in segmenting sarcomere images and in recognizing structurally abnormal areas, that characterize certain myopathies.

#### ACKNOWLEDGMENT

The authors would like to thank C. Mikellidou for assistance in preparing the electron micrographs.

#### REFERENCES

- [1] S. S. Schochet and W. D. Lampert, “Diagnostic electron microscopy of skeletal muscle,” in *Diagnostic Electron Microscopy*, B. F. Trump and R. T. Jones, Eds. New York: Wiley, 1978, pp. 209–252.
- [2] A. G. Engel and B. Q. Banker, “Ultrastructural changes in diseased muscle,” in *Myology: Basic and Clinical*, A. G. Engel and C. F. Armstrong, Eds. New York: McGraw-Hill, 1994, pp. 889–1017.
- [3] A. G. Engel, “Quantitative morphological studies of muscle,” in *Myology: Basic and Clinical*, A. G. Engel and C. F. Armstrong, Eds. New York: McGraw-Hill, 1994, pp. 1018–1045.
- [4] K. Kyriacou, B. Kassianides, and A. Hadjisavvas *et al.*, “The role of electron microscopy in the diagnosis of nonneoplastic muscle diseases,” *Ultrastruct. Pathol.*, vol. 21, pp. 243–252, 1997.

- [5] M. S. Pattichis, "AM-FM Transforms with Applications," Ph.D. dissertation, Univ. Texas, Austin, TX, 1998.
- [6] J. P. Havlicek, "AM-FM Image Models," Ph.D. dissertation, Univ. Texas, Austin, TX, 1996.
- [7] A. C. Bovik, N. Gopal, T. Emmoth, and A. Restrepo, "Localized measurement of emergent image frequencies by Gabor wavelets," *IEEE Trans. Inform. Theory (Special Issue on Wavelet Transforms and Multiresolution Signal Analysis)*, vol. 38, pp. 691-712, Mar. 1992.
- [8] A. C. Bovik, J. P. Havlicek, M. D. Desai, and D. S. Harding, "Limits on discrete modulated signals," *IEEE Trans. Signal Processing*, vol. 45, pp. 867-879, Apr. 1997.
- [9] J. Serra, *Image Analysis and Mathematical Morphology*. New York: Academic, 1982, vol. 1.
- [10] E. R. Dougherty, *An Introduction to Morphological Image Processing*. Bellingham, WA: SPIE Opt. Eng., 1992.
- [11] D. Schonfeld and J. Goutsias, "Optimal morphological pattern restoration from binary images," *IEEE Trans. Pattern Anal. Machine Intell.*, vol. 13, pp. 14-29, Jan. 1991.
- [12] K. Sivakumar, "Morphological analysis of random fields: Theory and applications," Ph.D. dissertation, Johns Hopkins Univ., Baltimore, MD, 1997.

## A Jini Service to Reconstruct Tomographic Data

Peter Knoll\*, E. Gröller, K. Höll, S. Mirzaei, K. Koriska, and H. Köhn

**Abstract**—Distributed computing that uses dynamic networks will change the way we work and communicate thanks to the interaction of devices and services, that are automatically added and removed from the network as needed. The Jini technology, which is built atop the Java programming language, provides a homogenous view of the network and extends the ability of code to migrate in Java. This software design model simplifies the configuration and access to hardware devices and software services in a network. Thus, it becomes possible to execute new services without pre-installing software on client machines. This new programming paradigm is especially important in medical applications, where the reliable transmission of information is essential. This paper demonstrates how single photon emission computerized tomography data can be iteratively reconstructed using a Jini service.

**Index Terms**—Distributed computing, Jini, nuclear medicine, reconstruction.

### I. INTRODUCTION

The commercial software used in our medical imaging departments is in general stored locally on image processing workstations. If such

Manuscript received February 28, 2000; revised September 24, 2000. The Associate Editor responsible for coordinating the review of this paper and recommending its publication was M. W. Vannier. *Asterisk indicates corresponding author.*

\*P. Knoll is with the Department of Nuclear Medicine, Wilhelminenspital, Montleartstr. 37, 1171 Vienna, and L. Boltzmann Institute of Nuclear Medicine, and also with the Department of Computer Graphics and Algorithms, Technical University of Vienna, Vienna, Austria (e-mail: Peter.Knoll@nuk.wil.mag-wien.gv.at).

E. Gröller is with Department of Computer Graphics and Algorithms, Technical University of Vienna, Vienna, Austria.

K. Höll and K. Koriska are with the Departments of Nuclear Medicine, Wilhelminenspital, Vienna, Austria.

S. Mirzaei and H. Köhn are with the Departments of Nuclear Medicine, Wilhelminenspital, and also with L. Boltzmann Institute of Nuclear Medicine, Vienna, Austria.

Publisher Item Identifier S 0278-0062(00)10789-X.

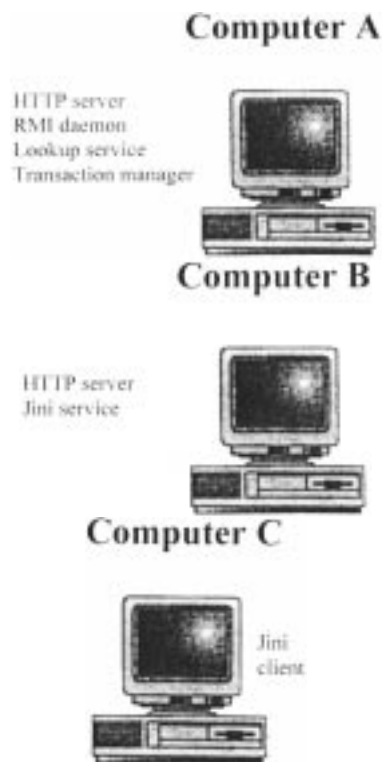


Fig. 1. Schematic presentation of the Jini concept.

a standalone application fails, processing terminates and remains unavailable until it is restarted. In contrast, distributed systems are able to tolerate a limited number of failures, since they consist of multiple independent processes. A distributed system has the advantage of easily supporting and coordinating remote access to patient data and software services. Although distributed medical image processing and viewing software uses the already existing client-server programming model [1], it lacks an important feature: A distributed system has to be able to adapt to network changes, which always will occur. In the future, services and devices will be dynamically added to and removed from computer networks, and it is necessary to adapt application software to this situation. Built on top of Java, object serialization and remote method invocation (RMI), the Jini application programming interface (API) [2] aims to extend the benefits of object-oriented programming to network enabling plugged-in devices and services to communicate through interfaces. Because Jini does not require centralized administration of available services, it is a truly distributed system [3].

Distributed Jini networks are customizable for a given user but can also add themselves automatically when powered up, and remove themselves when problems occur. This issue is important when software systems are intended to be long-lived entities that can stay running and responsive over a period of time, with little or no human intervention.

This paper describes the application of a Jini service, using as an example the reconstruction of single photon emission computed tomography (SPECT) data. The advantage to the physician of such an application is that he can change reconstruction parameters (such as number of iterations) during runtime using his own computer equipment (standard PC) and without prior knowledge of the implementation of the Jini service.